High-Order, Time-Dependent Aerodynamic Optimization using a Discontinuous Galerkin Discretization of the Navier-Stokes Equations

Matthew J. Zahr*
Stanford University, Stanford, CA 94305, U.S.A.
Per-Olof Persson†
University of California, Berkeley, Berkeley, CA 94720-3840, U.S.A.

The fully discrete adjoint method, corresponding to a globally high-order accurate discretization of the compressible Navier-Stokes equations on deforming domains, is introduced. A mapping-based Arbitrary Lagrangian-Eulerian description transforms the governing equations to a fixed reference domain. A high-order discontinuous Galerkin spatial discretization and diagonally implicit Runge-Kutta temporal discretization are employed to obtain the globally high-order discretization of the Navier-Stokes equations. Relevant quantities of interest, to be used as the objective function in aerodynamic trajectory optimization problems, are discretized in a solver-consistent manner. Gradients of these quantities of interest are computed via the adjoint method and verified against a second-order finite difference approximation. The proposed fully discrete adjoint method is coupled with state-of-the-art, gradient-based numerical optimization software to solve aerodynamic trajectory optimization problems. The first example is an inverse design problem with a known, global optimum that the solver is able to recover in fewer than 20 iterations. In a second problem, a trajectory is determined that successfully completes a prescribed mission while harvesting energy from the flow.

I. Introduction

Intrinsically time-dependent systems, where steady-state analysis in not applicable, constitute an important class of engineering problems. Such systems often arise in fluid dynamics for problems that are inherently dynamic, such as flapping flight, or problems where a steady-state solution does not exist, such as separated flow. Design or control of such systems calls for the solution of time-dependent PDE-constrained optimization problems of the form

$$\begin{aligned} \underset{\boldsymbol{U},\,\boldsymbol{\mu}}{\text{minimize}} \quad & \int_0^T \int_{\boldsymbol{\Gamma}} f(\boldsymbol{U}, \boldsymbol{\mu}, t)\, dS\, dt \\ \text{subject to} \quad & \frac{\partial \boldsymbol{U}}{\partial t} + \nabla \cdot \boldsymbol{F}(\boldsymbol{U}, \nabla \boldsymbol{U}) = 0 \end{aligned} \tag{1}$$

where the constraint corresponds to some vector-valued conservation law with solution $\boldsymbol{U}$, f is some output quantity of interest, and $\boldsymbol{\mu}$ are the optimization parameters. If a high degree of accuracy is sought, the numerical solution of such optimization problems with low-order methods may be an expensive endeavor.

This motivates the use of high-order methods, which have gained considerable attention for fluid problems due to their ability to produce highly accurate solutions with minimum numerical dispersion.[1,2] For PDE-constrained optimization, high-order convergence of integrated quantities of interest is sought as these

*Graduate Student, Institute for Computational and Mathematical Engineering, Stanford University, Stanford, CA 94035. E-mail: mzahr@stanford.edu. AIAA Student Member.
†Associate Professor, Department of Mathematics, University of California, Berkeley, Berkeley CA 94720-3840. E-mail: persson@berkeley.edu. AIAA Member.

quantities, and their gradients, drive an optimization algorithm, e.g. in the definition of the objective function and the constraints. This requires a *globally* high-order discretization of the governing, time-dependent PDE – the compressible Navier-Stokes equations, in this work. Additionally, a high-order numerical integration scheme is required for the quantities of interest whose dominant error term should match that of the discretization of the governing equation. This ensures high-order convergence in not only the solution of the partial differential equation, but in the quantities that drive the optimization.

In this work, a Discontinuous Galerkin (DG) method is used for the spatial discretization as it produces stable discretizations of the convective operator for arbitrarily high-order discretizations.[1] Diagonally Implicit Runge-Kutta (DIRK) schemes up to third-order are used for the temporal discretization. Two methods are considered for discretization of the integrated quantity of interest. Both methods approximate spatial integrals using the finite element shape functions of the discontinuous Galerkin scheme; they differ in their treatment of the temporal integrals. The first uses standard numerical quadrature rules, such as the trapezoidal rule or Simpson's rule. The second method applies the temporal discretization of the PDE to an augmented system of ODEs consisting of semi-discrete PDE and the output quantity. The advantage of this approach is the discretization of the output integral inherits the exact order of convergence of the temporal discretization.

Derivative computations are a crucial component of gradient-based PDE-constrained optimization. For time-dependent PDE-constrained optimization, three frameworks exist for defining derivatives of quantities of interest with respect to parameters, depending on whether the optimality system of (1) is posed at the continuous, semi-discrete, or fully discrete level. These constitute genuinely distinct methods for computing derivatives as it is well-documented that the operations of discretization and differentiation do not commute for finite spatial and temporal discretizations; see [3]. Since the fully discrete equations are being solved numerically, it is advantageous to pose the optimality system at the fully discrete level as this guarantees the computed gradients will be consistent with the functionals to which they correspond.[4] For the continuous and semi-discrete approaches, this will only be the case as the mesh size and time step approach zero. The fully discrete PDE-constrained optimization framework, which will be the focus of this document, is particularly important when high-order methods are used to discretize the time-dependent PDE since the mesh size and time step size are not necessarily small.

Equipped with the fully discrete high-order numerical scheme, the fully discrete PDE-constrained optimization problem is posed and the fully discrete, time-dependent adjoint method derived. From the dual variables, the gradient of the quantity of interest can be reconstructed at a cost essentially independent of the number of optimization parameters. The high-order numerical scheme and the corresponding fully discrete adjoint method are used to solve aerodynamic trajectory optimization problems using gradient-based optimization techniques.

The remainder of this document is organized as follows. Section II introduces the compressible Navier-Stokes equations and the isentropic assumption. This section also introduces the DG-ALE spatial discretization, the DIRK temporal discretization, and the discretization of the integrated quantities of interest. Section III presents the fully discrete adjoint method corresponding to the numerical scheme introduced in Section II. Section IV applies the high-order numerical scheme to optimize the trajectory of a 2D airfoil. Section V offers conclusions.

II. Governing Equations and Discretization

II.A. Partial Differential Equations

Consider the compressible Navier-Stokes equations, defined in the parametrized, time-dependent domain $v(\boldsymbol{\mu}, t)$,

$$\frac{\partial \rho}{\partial t} + \frac{\partial}{\partial x_i}(\rho u_i) = 0, \tag{2}$$

$$\frac{\partial}{\partial t}(\rho u_i) + \frac{\partial}{\partial x_i}(\rho u_i u_j + p) = +\frac{\partial \tau_{ij}}{\partial x_j} \quad \text{for } i = 1, 2, 3, \tag{3}$$

$$\frac{\partial}{\partial t}(\rho E) + \frac{\partial}{\partial x_i}\left(u_j(\rho E + p)\right) = -\frac{\partial q_j}{\partial x_j} + \frac{\partial}{\partial x_j}(u_j \tau_{ij}), \tag{4}$$

where ρ is the fluid density, u_1, u_2, u_3 are the velocity components, and E is the total energy. The viscous stress tensor and heat flux are given by

$$\tau_{ij} = \mu\left(\frac{\partial u_i}{\partial x_j} + \frac{\partial u_j}{\partial x_i} - \frac{2}{3}\frac{\partial u_k}{\partial x_j}\delta_{ij}\right) \qquad \text{and} \qquad q_j = -\frac{\mu}{\text{Pr}}\frac{\partial}{\partial x_j}\left(E + \frac{p}{\rho} - \frac{1}{2}u_k u_k\right). \tag{5}$$

Here, μ is the viscosity coefficient and $\text{Pr} = 0.72$ is the Prandtl number which we assume to be constant. For an ideal gas, the pressure p has the form

$$p = (\gamma - 1)\rho\left(E - \frac{1}{2}u_k u_k\right), \tag{6}$$

where γ is the adiabatic gas constant. In this work, the entropy is assumed constant, that is to say the flow is adiabatic and reversible. For a perfect gas, the entropy is defined as

$$s = p/\rho^\gamma. \tag{7}$$

Using (7) to explicitly relate the pressure and density, the energy equation becomes redundant. This effectively reduces the square system of PDEs of size $n_{sd} + 2$ to one of size $n_{sd} + 1$, where n_{sd} is the number of spatial dimensions. It can be shown, under suitable assumptions, that the solution of the isentropic approximation of the Navier-Stokes equations converges to the solution of the incompressible Navier-Stokes equations as the Mach number goes to 0.[5–7]

II.B. Spatial Discretization: Arbitrary Lagrangian-Eulerian Discontinuous Galerkin Method

In this work, a high-order Arbitrary Lagrangian-Eulerian (ALE) discontinuous Galerkin discretization of the Navier-Stokes equations on a deforming domain will be employed for the spatial discretization.[8,9] This is achieved by defining a time-dependent mapping from the physical domain to a *fixed* reference domain, where all computations will be performed.

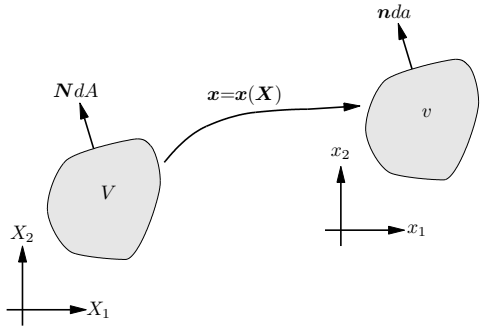

Figure 1: Time-dependent mapping between reference and physical domains.

Denote the physical domain by $v(\boldsymbol{\mu}, t) \subset \mathbb{R}^{n_{sd}}$ and the fixed, reference domain by $V \subset \mathbb{R}^{n_{sd}}$. At each time t, let $\mathcal{G}$ be a time-dependent diffeomorphism between the reference domain and physical domain: $\boldsymbol{x}(\boldsymbol{X}, \boldsymbol{\mu}, t) = \mathcal{G}(\boldsymbol{X}, \boldsymbol{\mu}, t)$, where $\boldsymbol{X} \in V$ is a point in the reference domain and $\boldsymbol{x}(\boldsymbol{X}, \boldsymbol{\mu}, t) \in v(\boldsymbol{\mu}, t)$ is the corresponding point in the physical domain at time t.

Consider the compressible Navier-Stokes equations in the physical domain $(\boldsymbol{x}, t)$, written as a system of conservation laws

$$\frac{\partial \boldsymbol{U}}{\partial t} + \nabla \cdot \boldsymbol{F}(\boldsymbol{U}, \nabla \boldsymbol{U}) = 0 \qquad \text{in } v(\boldsymbol{\mu}, t), \tag{8}$$

where $\boldsymbol{F}(\boldsymbol{U}, \nabla \boldsymbol{U}) = \boldsymbol{F}^{inv}(\boldsymbol{U}) + \boldsymbol{F}^{vis}(\boldsymbol{U}, \nabla \boldsymbol{U})$. For brevity, the transformed equations on the reference domain are stated without derivation,

$$\frac{\partial \boldsymbol{U}_{\boldsymbol{X}}}{\partial t} + \nabla_{\boldsymbol{X}} \cdot \boldsymbol{F}_{\boldsymbol{X}}(\boldsymbol{U}_{\boldsymbol{X}}, \nabla_{\boldsymbol{X}} \boldsymbol{U}_{\boldsymbol{X}}) = 0 \qquad \text{in } V, \tag{9}$$

where $\nabla_{\boldsymbol{X}}$ denotes spatial derivatives with respect to the reference variables, $\boldsymbol{X}$, and the transformed quantities take the form

$$\boldsymbol{U}_{\boldsymbol{X}} = \bar{g}\boldsymbol{U}, \qquad \boldsymbol{F}_{\boldsymbol{X}} = \boldsymbol{F}^{inv}_{\boldsymbol{X}} + \boldsymbol{F}^{vis}_{\boldsymbol{X}}, \qquad \boldsymbol{F}^{inv}_{\boldsymbol{X}} = g\boldsymbol{F}^{inv}\boldsymbol{G}^{-T} - \boldsymbol{U}_{\boldsymbol{X}} \otimes \boldsymbol{G}^{-1}\boldsymbol{v}_{\boldsymbol{G}}, \qquad \boldsymbol{F}^{vis}_{\boldsymbol{X}} = g\boldsymbol{F}^{vis}\boldsymbol{G}^{-T}, \tag{10}$$

where $\boldsymbol{G} = \nabla_{\boldsymbol{X}}\mathcal{G}$, $g = \det(\boldsymbol{G})$, and

$$\frac{\partial \bar{g}}{\partial t} - \nabla_{\boldsymbol{X}}(g\boldsymbol{G}^{-1}\boldsymbol{v}_{\boldsymbol{G}}) = 0. \tag{11}$$

This ALE formulation satisfies the Geometric Conservation Law (GCL),[10] as discussed in [9]. For details on the derivation, the reader is directed to [9].

With $\boldsymbol{U}_{\boldsymbol{X}}$ as the transformed variable, (9) can be converted to a first-order system

$$\begin{aligned} \frac{\partial \boldsymbol{U}_{\boldsymbol{X}}}{\partial t} + \nabla_{\boldsymbol{X}} \cdot \boldsymbol{F}_{\boldsymbol{X}}(\boldsymbol{U}_{\boldsymbol{X}}, \boldsymbol{Q}_{\boldsymbol{X}}) &= 0 \\ \boldsymbol{Q}_{\boldsymbol{X}} - \nabla_{\boldsymbol{X}}\boldsymbol{U}_{\boldsymbol{X}} &= 0 \end{aligned} \tag{12}$$

and discretized via a discontinuous Galerkin finite element method,[9] where the numerical fluxes used for the inviscid and viscous fluxes are the Roe flux[11] and Compact DG (CDG) flux,[12] respectively. The result of the discretization will be a system of Ordinary Differential Equations (ODEs), representing the semi-discretization of (12), the compressible Navier-Stokes equations on the *reference* domain,

$$\mathbb{M}\frac{\partial \boldsymbol{u}}{\partial t} = \boldsymbol{r}(\boldsymbol{u}, \boldsymbol{\mu}, t), \tag{13}$$

where $\mathbb{M}$ is the block-diagonal, symmetric, *fixed* mass matrix, $\boldsymbol{u}$ is the vectorization of $\boldsymbol{U}_{\boldsymbol{X}}$ at all nodes in the DG mesh, and $\boldsymbol{r}$ is the nonlinear function defining the DG discretization of the inviscid and viscous fluxes.

An important implication of performing all computations on a *fixed* reference domain is the mass matrix for the semi-discrete first-order system will be constant *for all times, t, and parameters,* $\boldsymbol{\mu}$. This has two primary benefits: (a) cost reduction as the mass matrix must be computed and factorized only once, and (b) simplification of the sensitivity/adjoint derivation as derivatives of mass matrix are zero, $\dfrac{\partial \mathbb{M}}{\partial \boldsymbol{\mu}} = 0$. This second point is particularly beneficial as both implementation and execution time are reduced since mass matrix sensitivities do not have to be derived, implemented, and computed.

With the high-order spatial discretization of the Navier-Stokes on a deformable domain defined, high-order temporal discretization of the resulting system of ODEs will be considered next.

II.C. Temporal Discretization: Diagonally Implicit Runge-Kutta

A subclass of the Implicit Runge-Kutta (IRK) schemes, known as Diagonally Implicit Runge-Kutta (DIRK) schemes,[13] are used for the temporal discretization. They are capable of achieving high-order, stable temporal discretizations without requiring the solution of an enlarged system of equations. The DIRK schemes are defined by a *lower triangular* Butcher tableau, that take the following form when applied to (13)

$$\begin{aligned} \boldsymbol{u}^{(n)} &= \boldsymbol{u}^{(n-1)} + \sum_{i=1}^{s} b_i \boldsymbol{k}_i^{(n)} \\ \mathbb{M}\boldsymbol{k}_i^{(n)} &= \Delta t_n \boldsymbol{r}\left(\boldsymbol{u}^{(n-1)} + \sum_{j=1}^{i} a_{ij}\boldsymbol{k}_j^{(n)},\ \boldsymbol{\mu},\ t_{n-1} + c_i \Delta t_n\right), \end{aligned} \tag{14}$$

for $n = 1, \ldots, N_t$ and $i = 1, \ldots, s$, where N_t are the number of time steps in the temporal discretization and s is the number of stages in the DIRK scheme. The temporal domain, $[0,\ T]$ is discretized into N_t segments with endpoints $\{t_0, t_1, \ldots, t_{N_t}\}$, with the nth segment having length $\Delta t_n = t_n - t_{n-1}$ for $n = 1, \ldots, N_t$.

From (14), a complete time step requires the solution of a sequence of s nonlinear systems of equation of size N. In Section IV, a third-order A- and L-stable DIRK scheme will be considered. The Butcher tableau for the DIRK scheme is given in Table 1.

II.D. Spatio-temporal Discretization of Quantities of Interest

The final discretization that must be considered is that of the integrated output quantity of interest

$$\mathcal{F}(\boldsymbol{U}, \boldsymbol{\mu}) = \int_0^T \int_{\boldsymbol{\Gamma}} f(\boldsymbol{U}, \boldsymbol{\mu}, t)\, dS\, dt. \tag{15}$$

α	α			
$\frac{1+\alpha}{2}$	$\frac{1+\alpha}{2}-\alpha$	α		
$\gamma+\omega+\alpha$	γ	ω	α	
	γ	ω	α	

Table 1: Butcher Tableau for 3-stage, 3rd order DIRK scheme
$\alpha = 0.435866521508459$, $\gamma = -\frac{6\alpha^2-16\alpha+1}{4}$, $\omega = \frac{6\alpha^2-20\alpha+5}{4}$

This output quantity may be either the objective function of the optimization problem of interest, *or a constraint*. The spatial integral is approximated with the shape functions of the finite element discretization

$$f_h(\boldsymbol{u}, \boldsymbol{\mu}, t) \approx \int_{\boldsymbol{\Gamma}} f(\boldsymbol{U}, \boldsymbol{\mu}, t)\, dS, \tag{16}$$

which is standard in the finite element community. In (16), f_h depends on the semi-discrete quantity $\boldsymbol{u}$ and approximates the continuous quantity $\displaystyle\int_{\boldsymbol{\Gamma}} f(\boldsymbol{U}, \boldsymbol{\mu}, t)\, dS$. Two high-order discretizations of the temporal integral in (15) are: (a) high-order numerical quadrature and (b) temporal discretization applied to an augmented system of ODEs. In the first case, the numerical approximation of $\mathcal{F}$ takes the form

$$\mathcal{F}(\boldsymbol{U}, \boldsymbol{\mu}) \approx F(\boldsymbol{u}^{(0)}, \ldots, \boldsymbol{u}^{(N_t)}, \boldsymbol{\mu}) = \sum_{i=0}^{N_t} w_i f_h(\boldsymbol{u}^{(i)}, \boldsymbol{\mu}, t_i), \tag{17}$$

where the weights, w_i, depend on the quadrature rule used. An important requirement on the choice of numerical quadrature is the nodes must align with time steps, which eliminates optimal numerical quadrature, such as Gauss-Legendre. Without this requirement, the solution must be interpolated to the quadrature nodes prior to application of (17).

A disadvantage of high-order numerical quadrature is the stencil expands as the approximation order increases. Additionally, when the system of ODEs are solved via an IRK scheme, there is additional information, namely the stages, $\boldsymbol{k}_i^{(n)}$, that are not being used in the output integration. An alternative that circumvents the disadvantages of high-order numerical quadrature is to apply the temporal discretization of the semi-discrete PDE to the following augmented system of ODEs,

$$\begin{bmatrix} \mathbb{M} & \mathbf{0} \\ \mathbf{0} & 1 \end{bmatrix} \begin{bmatrix} \dot{\boldsymbol{u}} \\ \dot{\mathcal{F}}_h \end{bmatrix} = \begin{bmatrix} \boldsymbol{r}(\boldsymbol{u}, \boldsymbol{\mu}, t) \\ f_h(\boldsymbol{u}, \boldsymbol{\mu}, t) \end{bmatrix}, \tag{18}$$

This method of integrating the output quantity of interest has the added benefits of ensuring the order of accuracy matches that of the time discretization. It would be unnecessary to integrate one more accurately than the other as the lowest order error term will dominate. Applying DIRK to equation (18), the following scheme is obtained

$$\begin{aligned} \boldsymbol{u}^{(n)} &= \boldsymbol{u}^{(n-1)} + \sum_{i=1}^{s} b_i \boldsymbol{k}_i^{(n)} \\ \mathcal{F}_h^{(n)} &= \mathcal{F}_h^{(n-1)} + \sum_{i=1}^{s} b_i f\left(\boldsymbol{u}^{(n-1)} + \sum_{j=1}^{i} a_{ij}\boldsymbol{k}_j^{(n)},\ \boldsymbol{\mu},\ t_{n-1} + c_i \Delta t_n\right) \\ \mathbb{M}\boldsymbol{k}_i^{(n)} &= \Delta t_n \boldsymbol{r}\left(\boldsymbol{u}^{(n-1)} + \sum_{j=1}^{i} a_{ij}\boldsymbol{k}_j^{(n)},\ \boldsymbol{\mu},\ t_{n-1} + c_i \Delta t_n\right). \end{aligned} \tag{19}$$

The output quantity of interest, $\mathcal{F}$ being sought will be approximated by

$$\mathcal{F}(\boldsymbol{U}, \boldsymbol{\mu}) \approx F(\boldsymbol{u}^{(0)}, \ldots, \boldsymbol{u}^{(N_t)}, \boldsymbol{k}_1^{(1)}, \ldots, \boldsymbol{k}_s^{(N_t)}, \boldsymbol{\mu}) = \mathcal{F}_h^{(N_t)}. \tag{20}$$

In the next section, the three high-order discretizations will be combined in the derivation of the fully discrete adjoint method for computing gradients of output quantities.

III. Fully Discrete, Time-Dependent Adjoint Method

In this section, the gradient of output functionals with respect to parameters are derived via a fully discrete, time-dependent adjoint method. Given the spatial and temporal discretization of the governing PDE, and the discretization of the integrated output quantity, the fully discrete, time-dependent PDE-constrained optimization problem is

$$\begin{aligned}
&\underset{\substack{\boldsymbol{u}^{(0)},\ \ldots,\ \boldsymbol{u}^{(N_t)}\in\mathbb{R}^{N_{\boldsymbol{u}}},\\ \boldsymbol{k}_1^{(1)},\ \ldots,\ \boldsymbol{k}_s^{(N_t)}\in\mathbb{R}^{N_{\boldsymbol{u}}},\\ \boldsymbol{\mu}\in\mathbb{R}^{N_{\boldsymbol{\mu}}}}}{\text{minimize}} && J(\boldsymbol{u}^{(0)},\ \ldots,\ \boldsymbol{u}^{(N_t)},\ \boldsymbol{k}_1^{(1)},\ \ldots,\ \boldsymbol{k}_s^{(N_t)},\ \boldsymbol{\mu}) \\
&\text{subject to} && \boldsymbol{u}^{(0)} = \boldsymbol{u}_0(\boldsymbol{\mu}) \\
& && \boldsymbol{u}^{(n)} = \boldsymbol{u}^{(n-1)} + \sum_{i=1}^{s} b_i \boldsymbol{k}_i^{(n)} \\
& && \mathbb{M}\boldsymbol{k}_i^{(n)} = \Delta t_n \boldsymbol{r}\left(\boldsymbol{u}^{(n-1)} + \sum_{j=1}^{i} a_{ij}\boldsymbol{k}_j^{(n)},\ \boldsymbol{\mu},\ t_{n-1} + c_i\Delta t_n\right)
\end{aligned} \tag{21}$$

where $i = \{1,\ldots,s\}$ and $n = \{1,\ldots,N_t\}$ in the constraints. For convenience, the following definitions are introduced

$$\begin{aligned}
\tilde{\boldsymbol{r}}^{(0)}(\boldsymbol{u}^{(0)},\boldsymbol{\mu}) &= \boldsymbol{u}^{(0)} - \boldsymbol{u}_0(\boldsymbol{\mu}) \\
\tilde{\boldsymbol{r}}^{(n)}(\boldsymbol{u}^{(n-1)},\boldsymbol{u}^{(n)},\boldsymbol{k}_1^{(n)},\ldots,\boldsymbol{k}_s^{(n)},\boldsymbol{\mu}) &= \boldsymbol{u}^{(n)} - \boldsymbol{u}^{(n-1)} - \sum_{i=1}^{s} b_i \boldsymbol{k}_i^{(i)} \\
\boldsymbol{R}^{(n)}(\boldsymbol{u}^{(n-1)},\boldsymbol{k}_1^{(n)},\ldots,\boldsymbol{k}_i^{(n)},\boldsymbol{\mu}) &= \mathbb{M}\boldsymbol{k}_i^{(n)} - \Delta t_n \boldsymbol{r}\left(\boldsymbol{u}^{(n-1)} + \sum_{j=1}^{i} a_{ij}\boldsymbol{k}_j^{(n)},\ \boldsymbol{\mu},\ t_{n-1} + c_i\Delta t_n\right).
\end{aligned} \tag{22}$$

The Lagrangian of the optimization problem in (21) takes the form

$$\begin{aligned}
&\mathcal{L}(\boldsymbol{u}^{(0)},\ \ldots,\ \boldsymbol{u}^{(N_t)},\ \boldsymbol{k}_1^{(1)},\ \ldots,\ \boldsymbol{k}_s^{(N_t)},\ \boldsymbol{\mu},\ \boldsymbol{\lambda}^{(0)},\ \ldots,\ \boldsymbol{\lambda}^{(N_t)},\ \boldsymbol{\kappa}_1^{(1)},\ \ldots,\ \boldsymbol{\kappa}_s^{(N_t)}) = \\
&\qquad J(\boldsymbol{u}^{(0)},\ \ldots,\ \boldsymbol{u}^{(N_t)},\ \boldsymbol{k}_1^{(1)},\ \ldots,\ \boldsymbol{k}_s^{(N_t)},\ \boldsymbol{\mu}) - \sum_{n=0}^{N_t} {\boldsymbol{\lambda}^{(n)}}^T \tilde{\boldsymbol{r}}^{(n)} - \sum_{n=0}^{N_t}\sum_{i=1}^{s} {\boldsymbol{\kappa}_i^{(n)}}^T \boldsymbol{R}_i^{(n)}.
\end{aligned} \tag{23}$$

The first-order optimality conditions of (21) state that the Lagrangian must be stationary at the optimal solution, i.e.

$$\begin{aligned}
\frac{\partial\mathcal{L}}{\partial\boldsymbol{u}^{(n)}} &= 0 && n = 0,\ldots,N_t \\
\frac{\partial\mathcal{L}}{\partial\boldsymbol{k}_i^{(n)}} &= 0 && i = 1,\ldots,s,\ n = 1,\ldots,N_t \\
\frac{\partial\mathcal{L}}{\partial\boldsymbol{\lambda}^{(n)}} &= 0 && n = 0,\ldots,N_t \\
\frac{\partial\mathcal{L}}{\partial\boldsymbol{\kappa}_i^{(n)}} &= 0 && i = 1,\ldots,s,\ n = 1,\ldots,N_t \\
\frac{\partial\mathcal{L}}{\partial\boldsymbol{\mu}} &= 0 && n = 0,\ldots,N_t.
\end{aligned} \tag{24}$$

Restricting attention to the variations with respect to the PDE state vectors, i.e. $\boldsymbol{u}^{(n)}$ and $\boldsymbol{k}_i^{(n)}$, the fully discrete adjoint evolution equations are obtained

$$
\begin{aligned}
\boldsymbol{\lambda}^{(N_t)} &= \frac{\partial J}{\partial \boldsymbol{u}^{(N_t)}}^T \\
\boldsymbol{\lambda}^{(n-1)} &= \boldsymbol{\lambda}^{(n)} + \frac{\partial J}{\partial \boldsymbol{u}^{(n-1)}}^T + \sum_{i=1}^{s} \Delta t_n \frac{\partial \boldsymbol{r}}{\partial \boldsymbol{u}} \left(\boldsymbol{u}^{(n-1)} + \sum_{j=1}^{i} a_{ij} \boldsymbol{k}_j^{(n)},\ \boldsymbol{\mu},\ t_{n-1} + c_i \Delta t_n \right)^T \boldsymbol{\kappa}_i^{(n)} \\
\mathbb{M}^T \boldsymbol{\kappa}_i^{(n)} &= \frac{\partial J}{\partial \boldsymbol{k}_i^{(n)}}^T + b_i \boldsymbol{\lambda}^{(n)} + \sum_{j=i}^{s} a_{ji} \Delta t_n \frac{\partial \boldsymbol{r}}{\partial \boldsymbol{u}} \left(\boldsymbol{u}^{(n-1)} + \sum_{q=1}^{j} a_{jq} \boldsymbol{k}_q^{(n)},\ \boldsymbol{\mu},\ t_{n-1} + c_j \Delta t_n \right)^T \boldsymbol{\kappa}_j^{(n)}
\end{aligned}
\tag{25}
$$

for $n = 1, \ldots, N_t$ and $i = 1, \ldots, s$. From the form of the discrete evolution equations in (25), the adjoint equations must be evolved *backward* in time, and the stages solved in *reverse* order. Furthermore, the adjoint equations can only be solved once the *primal* solution, $\boldsymbol{u}^{(n)}$ and $\boldsymbol{k}_i^{(n)}$, are available. This implies that the primal equations must be solved and the solution stored at each time step and each stage, prior to backward evolution of the adjoint equations.

Equipped with the primal solution, $\boldsymbol{u}^{(n)}$ and $\boldsymbol{k}_i^{(n)}$, and the dual solution, $\boldsymbol{\lambda}^{(n)}$ and $\boldsymbol{\kappa}_i^{(n)}$, the gradient of the functional can be computed as

$$
\frac{\mathrm{d}J}{\mathrm{d}\boldsymbol{\mu}} = \frac{\partial J}{\partial \boldsymbol{\mu}} + {\boldsymbol{\lambda}^{(0)}}^T \frac{\partial \boldsymbol{u}_0}{\partial \boldsymbol{\mu}} + \sum_{n=1}^{N_t} \Delta t_n \sum_{i=1}^{s} {\boldsymbol{\kappa}_i^{(n)}}^T \frac{\partial \boldsymbol{r}}{\partial \boldsymbol{\mu}} (\boldsymbol{u}_i^{(n)}, \boldsymbol{\mu}, t_{n-1} + c_i \Delta t_n); \tag{26}
$$

see [14] for the derivation. In the next section, the fully discrete adjoint method is used to compute the gradients of optimization functionals and solve for the optimal heaving motion of a 2D airfoil using gradient-based optimization.

IV. Application

IV.A. Problem Description

In this section, the fully discrete adjoint method corresponding to the high-order discretization of the conservation law and its quantities of interest is applied to solve PDE-constrained optimization problems. In particular, the optimal control of a 2D NACA0012 airfoil (Figure 2), with chord length $c = 1$ and zero-thickness trailing edge, is considered. The governing equations for this problem are the 2D compressible, isentropic Navier-Stokes equations.

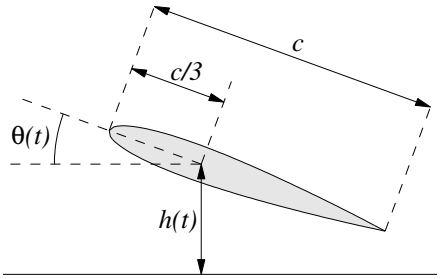

Figure 2: Schematic of geometry and kinematics of NACA0012 airfoil with zero-thickness trailing edge and cord length c. Only vertical translation, $h(t)$, and rotation about the 1/3-chord, $\theta(t)$, are permitted.

The mission of the airfoil is to move upward a distance of μ_1 in T units of time, smoothly varying its angle of attack from 0 at $t = 0$ to μ_2 at $t = T/2$ to 0 at $t = T$. Figure 2 illustrates the kinematically admissible motions of the airfoil, in terms of $h(t)$, the vertical translation of the airfoil, and $\theta(t)$, the rotation of the airfoil about the 1/3 chord, which coincides with the angle of attack since the incoming flow is perfectly

horizontal. The expressions for $h(t)$ and $\theta(t)$, in terms of the parameters μ_1 and μ_2 are given in (27)

$$h(t) = \begin{cases} 0, & \text{if } t < 0 \\ \mu_1 \frac{1-\cos \pi t/T}{2}, & 0 \le t < T \\ \mu_1, & \text{otherwise} \end{cases} \qquad \theta(t) = \begin{cases} 0, & \text{if } t < 0 \\ \mu_2 \cdot \frac{1-2\cos \pi t/T}{2}, & 0 \le t < T \\ 0, & \text{otherwise.} \end{cases} \tag{27}$$

The expressions for $h(t)$ and $\theta(t)$ ensure the motion is smooth ($h(t)$, $\theta(t)$ continuously differentiable) and slowly varying at the initial and final times ($h'(0) = h'(T) = \theta'(0) = \theta'(T) = 0$). They also guarantee the airfoil will begin at its nominal position ($y(0) = \theta(0) = 0$) and end at its target ($h(T) = \mu_1$, $\theta(T) = 0$). Finally, μ_2 is the amplitude of θ midway through the time interval ($\theta(T/2) = \mu_2$).

Seven output quantities of interest will be considered in this document. The first is the distance of the solution to the PDE at parameter $\boldsymbol{\mu}$, $\boldsymbol{U}(\boldsymbol{x}, \boldsymbol{\mu}, t)$, from a target state, $\boldsymbol{U}^*(\boldsymbol{x}, t)$,

$$\mathcal{I}(\boldsymbol{U}, \boldsymbol{\mu}, t) = \frac{1}{2} \int_0^T \int_{v(\boldsymbol{\mu},t)} |\boldsymbol{U}(\boldsymbol{x}, \boldsymbol{\mu}, t) - \boldsymbol{U}^*(\boldsymbol{x}, t)|^2 \, dv \, dt. \tag{28}$$

Here, the target state $\boldsymbol{U}^*(\boldsymbol{x}, t)$ corresponds to the solution of the partial differential equation at $\boldsymbol{\mu} = \boldsymbol{\mu}^* = [1.0,\ \pi/6]^T$. The fully discrete, high-order approximation to $\mathcal{I}(\boldsymbol{U}, \boldsymbol{\mu}, t)$ will be denoted $I(\boldsymbol{u}^{(0)}, \ldots, \boldsymbol{u}^{(N_t)}, \boldsymbol{k}_1^{(1)}, \ldots, \boldsymbol{k}_s^{(N_t)}, \boldsymbol{\mu})$. The remaining six quantities of interest for a body, defined by surface $\boldsymbol{\Gamma}$ (the airfoil surface, in this case), take the following form

$$\begin{aligned} \mathcal{F}_x(\boldsymbol{U}, \boldsymbol{\mu}, t) &= \int_{\boldsymbol{\Gamma}} \boldsymbol{f}(\boldsymbol{U}, \boldsymbol{\mu}, t) \cdot \boldsymbol{e}_1 \, dS & \mathcal{F}_y(\boldsymbol{U}, \boldsymbol{\mu}, t) &= \int_{\boldsymbol{\Gamma}} \boldsymbol{f}(\boldsymbol{U}, \boldsymbol{\mu}, t) \cdot \boldsymbol{e}_2 \, dS \\ \mathcal{T}_z(\boldsymbol{U}, \boldsymbol{\mu}, t) &= \int_{\boldsymbol{\Gamma}} \boldsymbol{f}(\boldsymbol{U}, \boldsymbol{\mu}, t) \times (\boldsymbol{x} - \boldsymbol{x}_0) \, dS & \mathcal{P}_y(\boldsymbol{U}, \boldsymbol{\mu}, t) &= \int_{\boldsymbol{\Gamma}} \dot{y} \boldsymbol{f}(\boldsymbol{U}, \boldsymbol{\mu}, t) \cdot \boldsymbol{e}_2 \, dS \\ \mathcal{P}_\theta(\boldsymbol{U}, \boldsymbol{\mu}, t) &= -\int_{\boldsymbol{\Gamma}} \dot{\theta} \boldsymbol{f}(\boldsymbol{U}, \boldsymbol{\mu}, t) \times (\boldsymbol{x} - \boldsymbol{x}_0) \, dS & \mathcal{P}(\boldsymbol{U}, \boldsymbol{\mu}, t) &= \int_{\boldsymbol{\Gamma}} \boldsymbol{f}(\boldsymbol{U}, \boldsymbol{\mu}, t) \cdot \dot{\boldsymbol{x}} \ \, dS \end{aligned} \tag{29}$$

where $\boldsymbol{f} \in \mathbb{R}^{n_{sd}}$ is the force imparted by fluid on the body, $\boldsymbol{e}_i$ is the ith canonical basis vector in $\mathbb{R}^{n_{sd}}$, $\boldsymbol{x}$ and $\dot{\boldsymbol{x}}$ are the position and velocity of a point on the surface $\boldsymbol{\Gamma}$, and y, θ, $\dot{y}$, $\dot{\theta}$ define the motion of the reference point, $\boldsymbol{x}_0$ (the 1/3-chord of the airfoil, in this case); see Figure 2. The $\mathcal{F}_x$ and $\mathcal{F}_y$ terms correspond to the total x- and y-directed forces on the body, $\mathcal{T}_z$ is the moment about $\boldsymbol{x}_0$, and $\mathcal{P}$ is the total power exerted on the body by the fluid. The total power $\mathcal{P}$ is broken into its translational, $\mathcal{P}_y$, and rotational, $\mathcal{P}_\theta$, components. For a 2D rigid body motion with no x-translation, an additive relationship among these terms holds

$$\mathcal{P}(\boldsymbol{U}, \boldsymbol{\mu}, t) = \mathcal{P}_y(\boldsymbol{U}, \boldsymbol{\mu}, t) + \mathcal{P}_\theta(\boldsymbol{U}, \boldsymbol{\mu}, t). \tag{30}$$

The negative sign is included in the definition of $\mathcal{P}_\theta$ due to the clockwise definition of θ in Figure 2. In the remainder of this document, a superscript h will be used to denote the high-order DG approximation to these spatial integrals that constitute the instantaneous quantities of interest, e.g., $\mathcal{P}^h(\boldsymbol{u}, \boldsymbol{\mu}, t)$ is the high-order approximation of $\mathcal{P}(\boldsymbol{U}, \boldsymbol{\mu}, t)$, where $\boldsymbol{u}$ is the semi-discrete approximation of $\boldsymbol{U}$. Temporal integration of the instantaneous quantities of interest leads to the integrated quantities of interest

$$\begin{aligned} \mathcal{J}_x(\boldsymbol{U}, \boldsymbol{\mu}) &= \int_0^T \int_{\boldsymbol{\Gamma}} \boldsymbol{f}(\boldsymbol{U}, \boldsymbol{\mu}, t) \cdot \boldsymbol{e}_1 \, dS \, dt & \mathcal{J}_y(\boldsymbol{U}, \boldsymbol{\mu}) &= \int_0^T \int_{\boldsymbol{\Gamma}} \boldsymbol{f}(\boldsymbol{U}, \boldsymbol{\mu}, t) \cdot \boldsymbol{e}_2 \, dS \, dt \\ \mathcal{J}_\theta(\boldsymbol{U}, \boldsymbol{\mu}) &= \int_0^T \int_{\boldsymbol{\Gamma}} \boldsymbol{f}(\boldsymbol{U}, \boldsymbol{\mu}, t) \times (\boldsymbol{x} - \boldsymbol{x}_0) \, dS \, dt & \mathcal{W}_y(\boldsymbol{U}, \boldsymbol{\mu}) &= \int_0^T \int_{\boldsymbol{\Gamma}} \dot{y} \boldsymbol{f}(\boldsymbol{U}, \boldsymbol{\mu}, t) \cdot \boldsymbol{e}_2 \, dS \, dt \\ \mathcal{W}_\theta(\boldsymbol{U}, \boldsymbol{\mu}) &= -\int_0^T \int_{\boldsymbol{\Gamma}} \dot{\theta} \boldsymbol{f}(\boldsymbol{U}, \boldsymbol{\mu}, t) \times (\boldsymbol{x} - \boldsymbol{x}_0) \, dS \, dt & \mathcal{W}(\boldsymbol{U}, \boldsymbol{\mu}) &= \int_0^T \int_{\boldsymbol{\Gamma}} \boldsymbol{f}(\boldsymbol{U}, \boldsymbol{\mu}, t) \cdot \dot{\boldsymbol{x}} \, dS \, dt, \end{aligned} \tag{31}$$

which will be used as optimization functionals in subsequent sections. The terms $\mathcal{J}_x$, $\mathcal{J}_y$, and $\mathcal{J}_\theta$ are the x-, y-directed, and rotational impulse the fluid exerts on the airfoil, respectively. $\mathcal{W}$ is the total work done on the airfoil by the fluid and $\mathcal{W}_y$ and $\mathcal{W}_\theta$ are its translational and rotational components. The fully discrete, high-order approximation of the integrated quantities of interest (DG-in-space, DIRK-in-time) will be denoted with the corresponding Roman symbol, e.g., $W(\boldsymbol{u}^{(0)}, \ldots, \boldsymbol{u}^{(N_t)}, \boldsymbol{k}_1^{(n)}, \ldots, \boldsymbol{k}_s^{(n)}, \boldsymbol{\mu})$ is the fully discrete approximation of $\mathcal{W}(\boldsymbol{U}, \boldsymbol{\mu})$.

Before considering an unsteady optimization problem, the derivatives obtained via the fully discrete adjoint method of Section III are compared to finite differences. To minimize the effect of catastrophic cancellation, a centered finite difference scheme is utilized. Figure 3 shows the discrepancy between the gradient computed via the fully discrete adjoint method and that computed via finite differences is small ($\mathcal{O}(10^{-7})$) for two of the output quantities of interest.

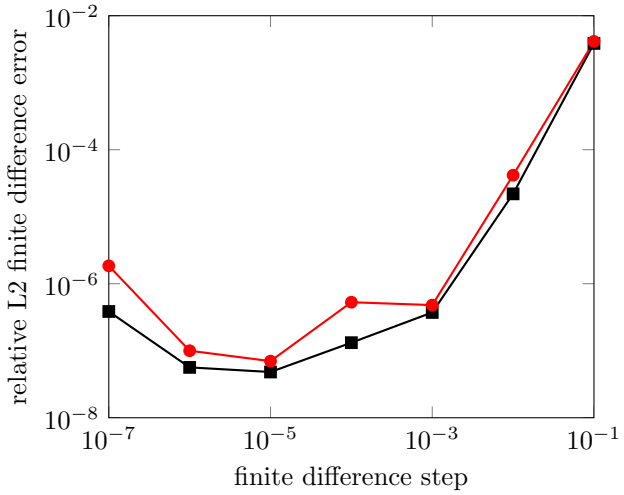

Figure 3: Comparison of $\frac{\mathrm{d}I}{\mathrm{d}\boldsymbol{\mu}}$ (—■—) and $\frac{\mathrm{d}W}{\mathrm{d}\boldsymbol{\mu}}$ (—●—) computed from fully discrete adjoint method with that obtained from second-order finite difference approximation, for various step sizes.

The next sections will consider time-dependent optimization and control problems using the quantities of interest from (28) and (31) as optimization functionals.

IV.B. Aerodynamic Inverse Design

In this section, an inverse design problem is considered, where a target solution $\boldsymbol{U}^*(\boldsymbol{x},t)$ is obtained by solving (14) at $\boldsymbol{\mu}=\boldsymbol{\mu}^*$, then $\mathcal{I}$ is minimized to recover $\boldsymbol{\mu}^*$ by only considering $\boldsymbol{U}^*(\boldsymbol{x},t)$. The fully discrete version of this problem takes the form

$$
\begin{aligned}
\underset{\substack{\boldsymbol{u}^{(0)},\ \ldots,\ \boldsymbol{u}^{(N_t)}\in\mathbb{R}^{N_{\boldsymbol{u}}},\\ \boldsymbol{k}_1^{(1)},\ \ldots,\ \boldsymbol{k}_s^{(N_t)}\in\mathbb{R}^{N_{\boldsymbol{u}}},\\ \boldsymbol{\mu}\in\mathbb{R}^{N_{\boldsymbol{\mu}}}}}{\text{minimize}} \quad & I(\boldsymbol{u}^{(0)},\ldots,\boldsymbol{u}^{(N_t)},\boldsymbol{k}_1^{(1)},\ldots,\boldsymbol{k}_s^{(N_t)},\boldsymbol{\mu}) \\
\text{subject to} \quad & -2.0\leq\mu_1\leq 2.0, \quad -\pi/2\leq\mu_2\leq\pi/2 \\
& \boldsymbol{u}^{(0)}=\boldsymbol{u}_0 \\
& \boldsymbol{u}^{(n)}=\boldsymbol{u}^{(n-1)}+\sum_{i=1}^{s} b_i\boldsymbol{k}_i^{(n)} \\
& \mathbb{M}\boldsymbol{k}_i^{(n)}=\Delta t_n\boldsymbol{r}\left(\boldsymbol{u}_i^{(n)},\ \boldsymbol{\mu},\ t_{n-1}+c_i\Delta t_n\right).
\end{aligned}
\tag{32}
$$

The spatial discretization of the compressible Navier-Stokes equations uses the DG-ALE formulation from Section II.B with 971 $p=3$ elements. The time interval of $T=2$ is discretized via DIRK3 with 100 time steps and Simpson's rule is used to discretize $\mathcal{I}$ as I. The Reynolds number for the flow is 100 and the Mach number is 0.2. All unsteady CFD simulations are initialized from the steady-state solution of the $t=0$ configuration of the airfoil. The airfoil trajectory is discretized according to (27) and the target solution corresponds to the parameter $\mu_1^*=1.0$, $\mu_2^*=\pi/6$.

The L-BFGS-B[15] solver is used to solve (32), a bound-constrained optimization problem with a nonlinear objective function. The gradients of the objective function with respect to parameter, $\dfrac{\mathrm{d}I}{\mathrm{d}\boldsymbol{\mu}}$, are computed via the fully discrete adjoint method according to Section III. The convergence of the optimization procedure is contained in Figure 4, which shows the decay of the objective function to zero in 20 iterations. This indicates

that the optimizer found a parameter that recovers the target state. Figure 4 also shows the evolution of μ_1 and μ_2 as a function of iteration, from which it is can be verified the optimizer recovers the target parameters, μ_1^* and μ_2^*.

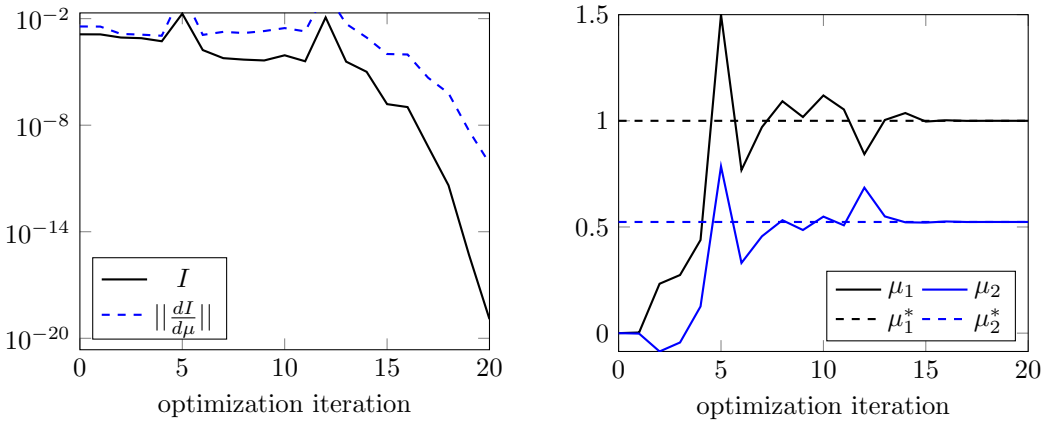

Figure 4: Convergence history for inverse design optimization problem.

IV.C. Energetically Optimal Trajectory

In this section, the problem of determining the energetically optimal trajectory of a 2D NACA0012 airfoil with chord length $c = 1$ and zero-thickness trailing edge is considered. The fully discrete version of this problem takes the form

$$\begin{aligned} \underset{\substack{\boldsymbol{u}^{(0)},\ \ldots,\ \boldsymbol{u}^{(N_t)}\in\mathbb{R}^{N_{\boldsymbol{u}}},\\ \boldsymbol{k}_1^{(1)},\ \ldots,\ \boldsymbol{k}_s^{(N_t)}\in\mathbb{R}^{N_{\boldsymbol{u}}},\\ \boldsymbol{\mu}\in\mathbb{R}^{N_{\boldsymbol{\mu}}}}}{\text{minimize}} \quad & W(\boldsymbol{u}^{(0)},\ldots,\boldsymbol{u}^{(N_t)},\boldsymbol{k}_1^{(1)},\ldots,\boldsymbol{k}_s^{(N_t)},\boldsymbol{\mu}) \\ \text{subject to} \quad & \boldsymbol{u}^{(0)} = \boldsymbol{u}_0 \\ & \boldsymbol{u}^{(n)} = \boldsymbol{u}^{(n-1)} + \sum_{i=1}^{s} b_i \boldsymbol{k}_i^{(n)} \\ & \mathbb{M}\boldsymbol{k}_i^{(n)} = \Delta t_n \boldsymbol{r}\left(\boldsymbol{u}_i^{(n)},\ \boldsymbol{\mu},\ t_{n-1} + c_i \Delta t_n\right). \end{aligned} \tag{33}$$

The spatial discretization of the compressible Navier-Stokes equations uses the DG-ALE formulation from Section II.B with 971 $p = 3$ elements. The time interval of $T = 2$ is discretized via DIRK3 with 100 time steps and the solver consistent discretization is used for the output integral. The Reynolds number for the flow is 1000 and the Mach number is 0.2. All unsteady CFD simulations are initialized from the steady-state solution of the $t = 0$ configuration of the airfoil. Similar to the previous section, the prescribed mission for the airfoil is to begin at the nominal position, $y(0) = \theta(0) = 0$, and end at $y(T) = 1.0$ and $\theta(T) = 0$.

The trajectory of the airfoil – $y(t)$ and $\theta(t)$ – is discretized via clamped cubic splines with m_y+1 and $m_\theta+1$ knots, respectively. The knots are uniformly spaced between 0 and T in the t-dimension and the knot values are optimization parameters. The derivatives of $y(t)$ and $\theta(t)$ are clamped to zero at the endpoints of the time interval to ensure smooth transitions and avoid non-physical transients. Two instances of the optimization problem in (33), corresponding to different parametrizations, will be considered. Parametrization PI will fix the translational motion and optimize over only the rotation, while PII will optimize over both the translational and rotational motion; see Table 2. Given the generality of this spline discretization, bound constraints were added to (33) to ensure reasonable motions of the airfoil are obtained.

Similar to the inverse design problem in the previous section, the L-BFGS-B solver is applied to (33) to solve the bound-constrained optimization problem with a nonlinear objective. The gradients of the objective function with respect to parameter, $\dfrac{\mathrm{d}W}{\mathrm{d}\boldsymbol{\mu}}$, are computed using the fully discrete adjoint method, which was verified against a second-order finite difference approximation in Figure 3.

PI			PII		
m_y	m_θ	$N_{\boldsymbol{\mu}}$	m_y	m_θ	$N_{\boldsymbol{\mu}}$
0	5	6	5	5	12

Table 2: Summary of parametrizations considered in Section IV.C. The number of clamped cubic spline knots used to discretize $y(t)$ and $\theta(t)$ are m_y+1 and $m_\theta+1$, respectively. PI freezes the rigid body translation ($m_y = 0$) and optimizes over only the rotation ($m_\theta \neq 0$). PII optimizes over all rigid body degrees of freedom ($m_y = m_\theta \neq 0$).

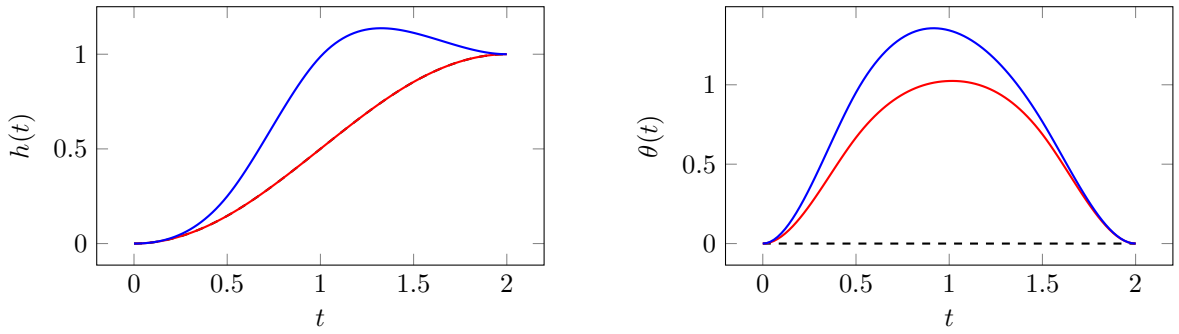

Figure 5: Trajectories of $y(t)$ and $\theta(t)$ at initial guess (- - -), energetically optimal pitch at fixed translation - PI (——), and energetically optimal pitch and translation - PII (——).

A summary of the optimal trajectory for both parametrizations is provided in Figure 5. Optimization under parametrization PI introduces pitch to the trajectory and PII introduces an *overshoot* in the vertical translation and further increases the pitch. The vorticity of the flow corresponding to the initial guess (pure heave), optimal solution under parametrization PI, and optimal solution under PII are shown in Figures 8 - 10, respectively. The incorporation of pitch in PI and vertical overshoot in PII confines all separation to the end of the time interval. This also causes the net force on the airfoil and its motion to be aligned for a portion of the trajectory, leading to an instantaneous extraction of power, which can be verified in Figure 7. For parametrization PI, the integrated result is an order of magnitude decrease in the total work required to complete the mission; see Figure 6. In contrast, the optimal solution under parametrization PII *extracts* or harvests energy from the flow, which can also be verified in Figure 6.

The convergence of all quantities of interest with optimization iteration is shown in Figure 6 for parametrizations PI and PII. The optimization problem in (33) under parametrization PI effectively converges in fewer than 20 iterations, while the larger design space of parametrization PII required about 40 iterations. The auxiliary quantities of interest – those not included as optimization functionals – were included to emphasize that the energy reduction was performed without consideration of these quantities. For example, the reduction in the energy was accompanied with a large increase in the drag (F_x) and moment (T_z) on the airfoil.

The time history of all instantaneous quantities of interest are shown at the initial guess and optimal solution of (33) under parametrizations PI and PII in Figure 7. It can be seen that the optimized motions extract a large amount of power from the flow during the middle of the time interval (approximately $t = 0.5$ to $t = 1.5$) at the cost of a large amount of input power at the edges of the interval to conform to the imposed boundary conditions on $y(t)$ and $\theta(t)$. The uncontrolled quantities of interest, such as the forces and torque, substantially increase in magnitude; a side-effect of the energy reductions and extraction.

V. Conclusion

This work introduces a *globally* high-order accurate numerical scheme for the solution of the compressible Navier-Stokes equations on a deformable domain. The adjoint equations of the *fully discrete* numerical scheme derived and the gradient of (integrated) quantities of interest are expressed in terms of the primal and dual solutions of the numerical scheme. The numerical scheme is defined by a high-order Discontinuous

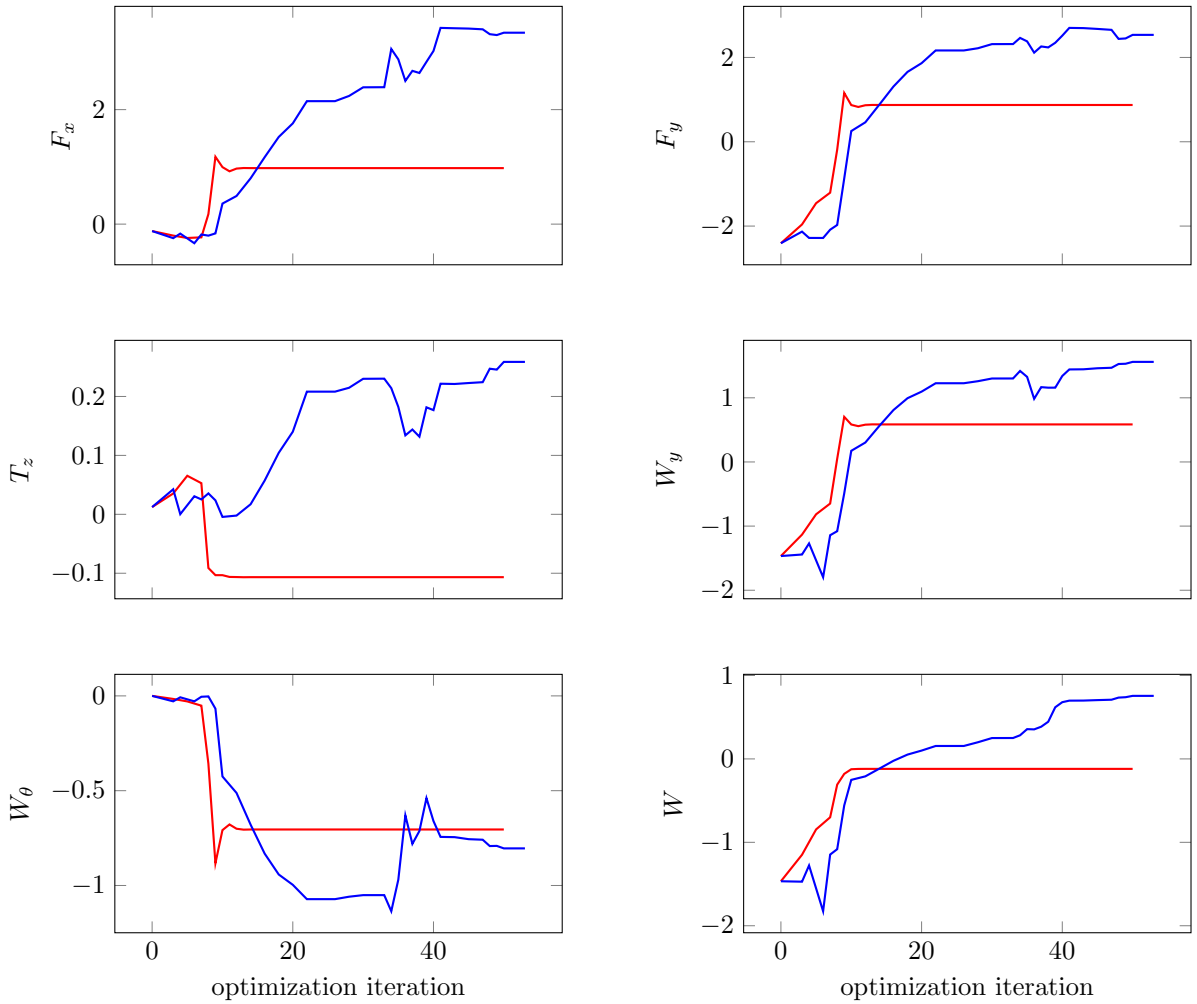

Figure 6: Optimization convergence of integrated quantities of interest (x-directed impulse – J_x, y-directed impulse – J_y, rotational impulse – J_θ, y-translational work – W_y, rotational work – W_θ, total work – W) for problem (33) under parametrizations PI (——) and PII (——).

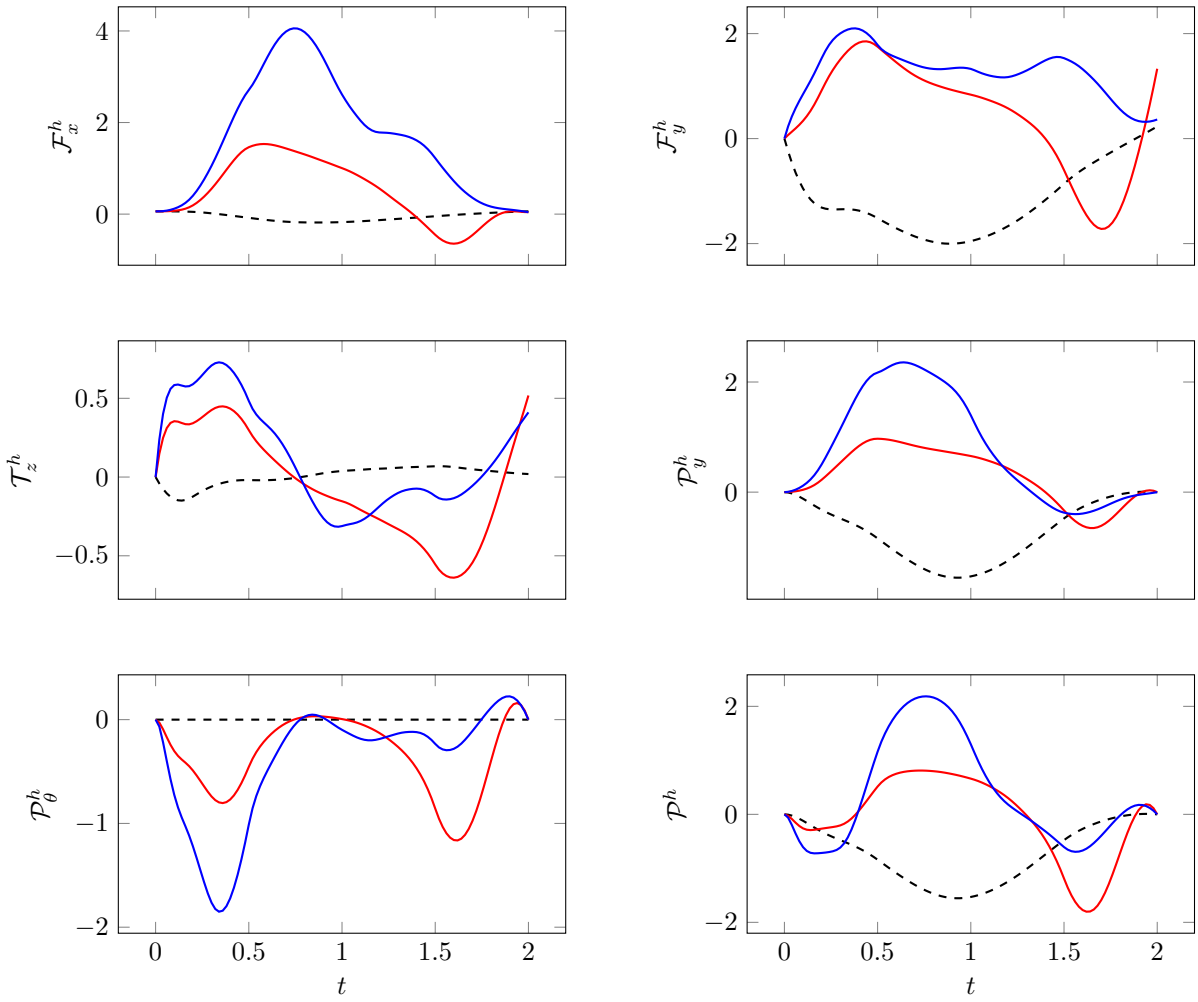

Figure 7: Time history of instantaneous quantities of interest (x-directed force – $\mathcal{F}_x^h(\boldsymbol{u}, \boldsymbol{\mu}, t)$, y-directed force – $\mathcal{F}_y^h(\boldsymbol{u}, \boldsymbol{\mu}, t)$, torque – $\mathcal{T}_z^h(\boldsymbol{u}, \boldsymbol{\mu}, t)$, y-translational power – $\mathcal{P}_y^h(\boldsymbol{u}, \boldsymbol{\mu}, t)$, rotational power – $\mathcal{P}_\theta^h(\boldsymbol{u}, \boldsymbol{\mu}, t)$, total power – $\mathcal{P}^h(\boldsymbol{u}, \boldsymbol{\mu}, t)$) at initial guess (- - -), solution of (33) under parametrization PI (——), and solution of (33) under parametrization PII (——).

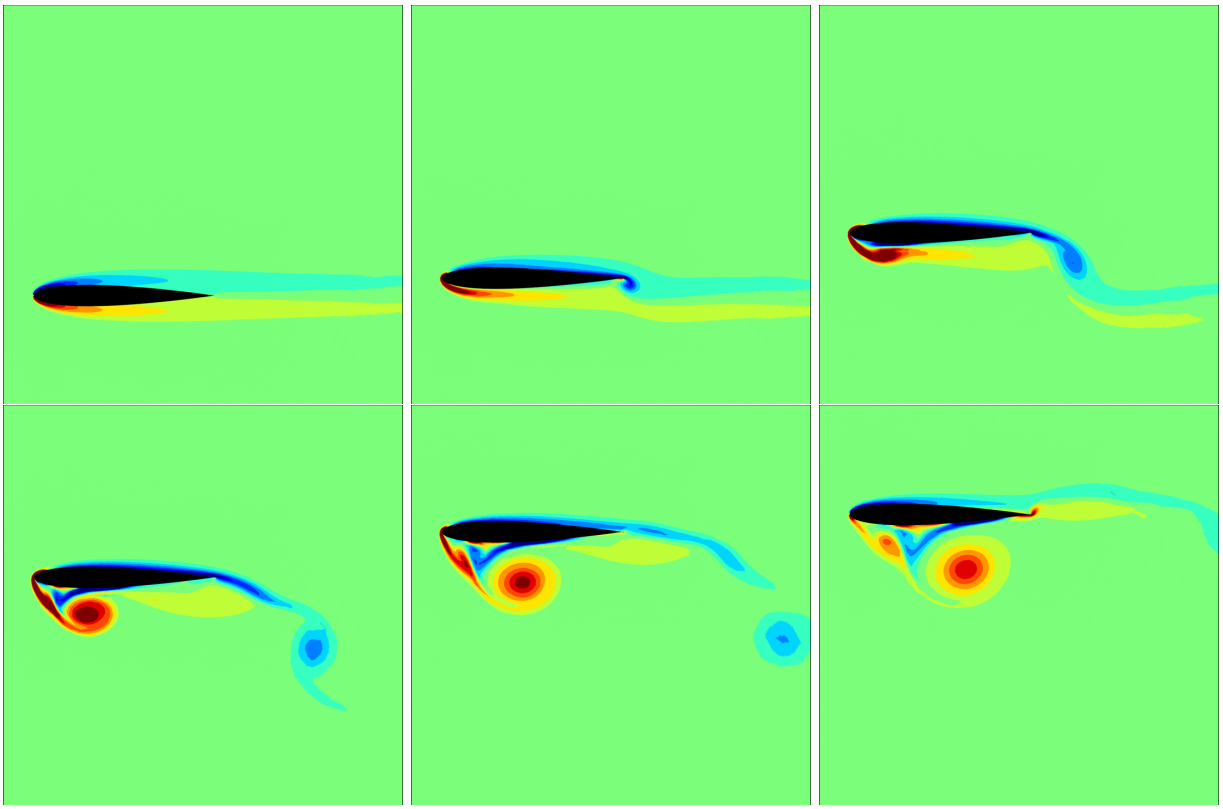

Figure 8: Flow vorticity around flapping airfoil undergoing motion corresponding to initial guess for optimization problem (33), i.e., pure heave (- - -). Flow separation off leading edge implies a large amount of work required to complete mission. Snapshots taken at times $t = 0.0,\ 0.4,\ 0.8,\ 1.2,\ 1.6,\ 2.0$.

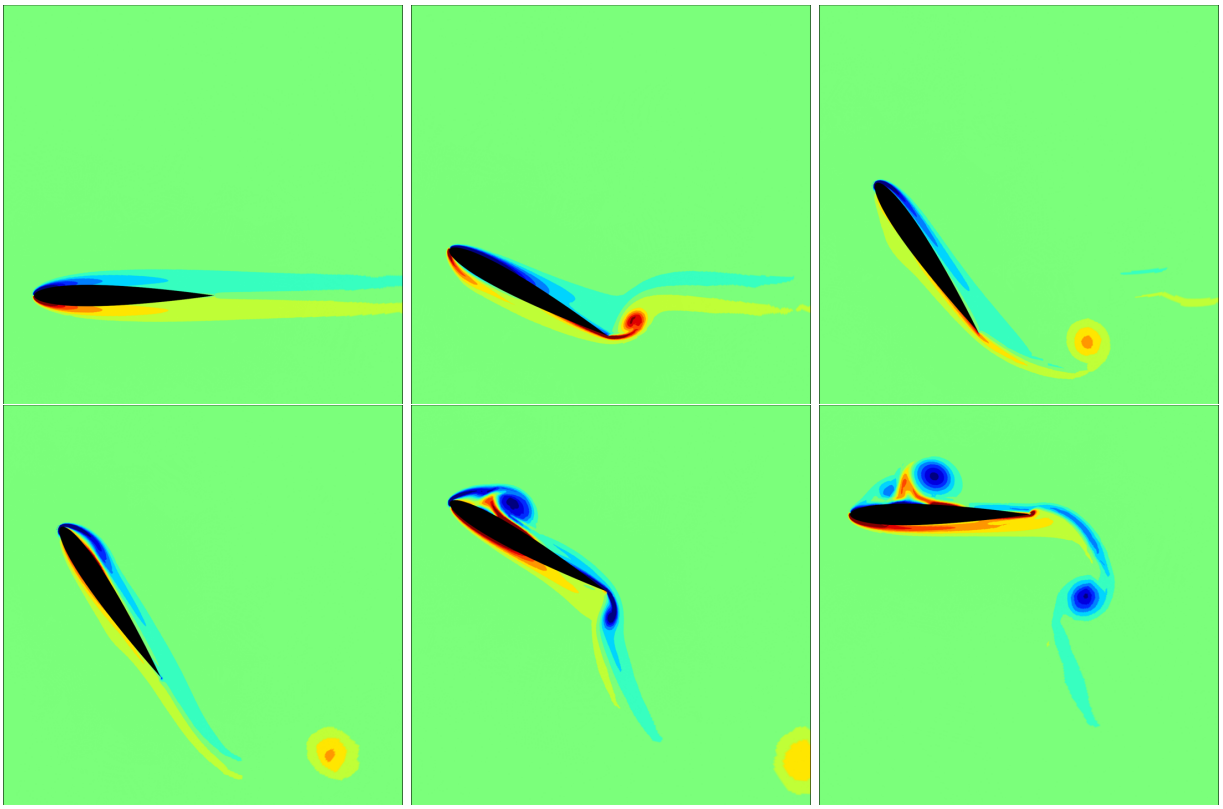

Figure 9: Flow vorticity around airfoil undergoing energetically optimal pitching motion for the fixed translational motion in Figure 5 (- - -). The pitching motion limits the flow separation to the end of the trajectory and results in a reduction of required energy to complete mission. Snapshots taken at times $t = 0.0,\ 0.4,\ 0.8,\ 1.2,\ 1.6,\ 2.0$.

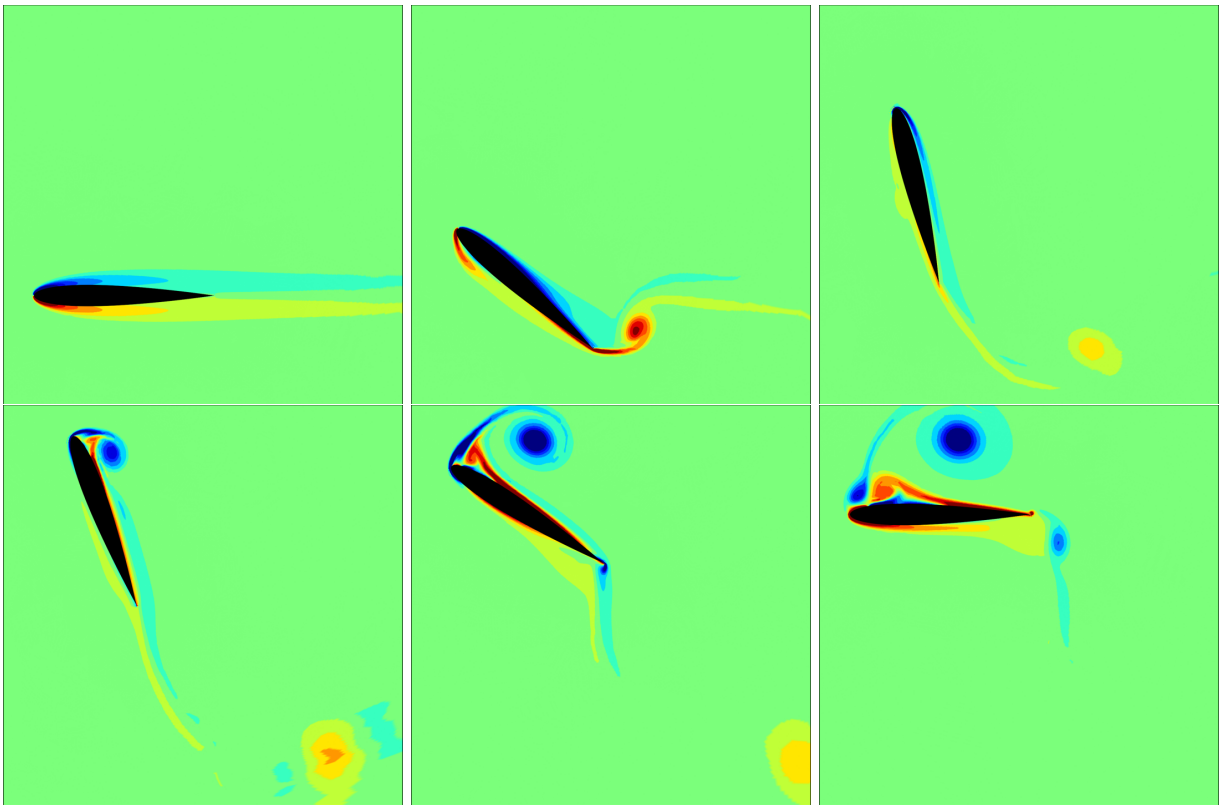

Figure 10: Flow vorticity around airfoil undergoing energetically optimal rigid body motion. The modified pitching and heaving trajectories result in energy *extraction* since the resultant force on the airfoil and its velocity are in the same direction for a large portion of the motion. Snapshots taken at times $t = 0.0,\ 0.4,\ 0.8,\ 1.2,\ 1.6,\ 2.0$.

Galerkin Arbitrary Lagrangian-Eulerian spatial discretization and Diagonally Implicit Runge-Kutta temporal discretization. The fully discrete adjoint method ensures the gradients of the quantities of interest are *consistent* with the functionals themselves.

The quantity of interest gradients were shown to closely match the gradients obtained via finite differences, validating the fully discrete adjoint method. The high-order scheme was applied to solve a time-dependent aerodynamic optimal control problems using *gradient-based* optimization. For an inverse design problem, the target control was recovered, to machine precision, in about 20 optimization iterations. The framework was also used to determine the energetically optimal trajectory of an airfoil in viscous, compressible flow. Even given a poor initial trajectory for the optimization problem that required a large amount of energy to complete, the optimal trajectory was able to *extract* energy from the flow.

Acknowledgments

This work was supported by the Department of Energy Computational Science Graduate Fellowship Program of the Office of Science and National Nuclear Security Administration in the Department of Energy under contract DE-FG02-97ER25308, and by the Director, Office of Science, Computational and Technology Research, U.S. Department of Energy under Contract No. DE-AC02-05CH11231. The content of this publication does not necessarily reflect the position or policy of any of these supporters, and no official endorsement should be inferred.

References

[1]Wang, Z., Fidkowski, K., Abgrall, R., Bassi, F., Caraeni, D., Cary, A., Deconinck, H., Hartmann, R., Hillewaert, K., Huynh, H., et al., "High-order CFD methods: current status and perspective," *International Journal for Numerical Methods in Fluids*, Vol. 72, No. 8, 2013, pp. 811–845.

[2]Zahr, M. J. and Persson, P.-O., *Performance tuning of Newton-GMRES methods for discontinuous Galerkin discretizations of the Navier-Stokes equations*, American Institute of Aeronautics and Astronautics, 2015/06/24 2013.

[3]Gunzburger, M. D., *Perspectives in flow control and optimization*, Vol. 5, Siam, 2003.

[4]Mader, C. A., RA Martins, J., Alonso, J. J., and Der Weide, E. V., "ADjoint: An approach for the rapid development of discrete adjoint solvers," *AIAA journal*, Vol. 46, No. 4, 2008, pp. 863–873.

[5]Lin, C.-K., "On the incompressible limit of the compressible Navier-Stokes equations," *Communications in partial differential equations*, Vol. 20, No. 3-4, 1995, pp. 677–707.

[6]Desjardins, B., Grenier, E., Lions, P.-L., and Masmoudi, N., "Incompressible Limit for Solutions of the Isentropic Navier–Stokes Equationswith Dirichlet Boundary Conditions," *Journal de Mathématiques Pures et Appliquées*, Vol. 78, No. 5, 1999, pp. 461–471.

[7]Froehle, B. M., *High-order discontinuous Galerkin fluid-structure interaction methods*, University of California, Berkeley, 2013.

[8]Persson, P.-O., Peraire, J., and Bonet, J., "A high order discontinuous Galerkin method for fluid-structure interaction," *18th AIAA Computational Fluid Dynamics Conference*, 2007.

[9]Persson, P.-O., Bonet, J., and Peraire, J., "Discontinuous Galerkin solution of the Navier–Stokes equations on deformable domains," *Computer Methods in Applied Mechanics and Engineering*, Vol. 198, No. 17, 2009, pp. 1585–1595.

[10]Farhat, C., Geuzaine, P., and Grandmont, C., "The discrete geometric conservation law and the nonlinear stability of ALE schemes for the solution of flow problems on moving grids," *Journal of Computational Physics*, Vol. 174, No. 2, 2001, pp. 669–694.

[11]Roe, P. L., "Approximate Riemann solvers, parameter vectors, and difference schemes," *Journal of computational physics*, Vol. 43, No. 2, 1981, pp. 357–372.

[12]Peraire, J. and Persson, P.-O., "The compact discontinuous Galerkin (CDG) method for elliptic problems," *SIAM Journal on Scientific Computing*, Vol. 30, No. 4, 2008, pp. 1806–1824.

[13]Alexander, R., "Diagonally implicit Runge-Kutta methods for stiff o.d.e.'s," *SIAM J. Numer. Anal.*, Vol. 14, No. 6, 1977, pp. 1006–1021.

[14]Zahr, M. J. and Persson, P.-O., "An Adjoint Method for a High-Order Discretization of Deforming Domain Conservation Laws for Optimization of Flow Problems," *Journal of Computational Physics*, 2016.

[15]Zhu, C., Byrd, R. H., Lu, P., and Nocedal, J., "Algorithm 778: L-BFGS-B: Fortran subroutines for large-scale bound-constrained optimization," *ACM Transactions on Mathematical Software (TOMS)*, Vol. 23, No. 4, 1997, pp. 550–560.